



HAL
open science

Spin-valley coupling enhanced high-TC ferromagnetism in a non-van der Waals monolayer Cr₂Se₃ on graphene

Chien-Wen Chuang, Tappei Kawakami, Katsuaki Sugawara, Kosuke Nakayama, Seigo Souma, Miho Kitamura, Kenta Amemiya, Koji Horiba, Hiroshi Kumigashira, Geoffroy Kremer, et al.

► To cite this version:

Chien-Wen Chuang, Tappei Kawakami, Katsuaki Sugawara, Kosuke Nakayama, Seigo Souma, et al.. Spin-valley coupling enhanced high-TC ferromagnetism in a non-van der Waals monolayer Cr₂Se₃ on graphene. Nature Communications, 2025, 16, <10.1038/s41467-025-58643-3>. <hal-05047482>

HAL Id: hal-05047482

<https://hal.science/hal-05047482v1>

Submitted on 25 Apr 2025

HAL is a multi-disciplinary open access archive for the deposit and dissemination of scientific research documents, whether they are published or not. The documents may come from teaching and research institutions in France or abroad, or from public or private research centers.

L'archive ouverte pluridisciplinaire HAL, est destinée au dépôt et à la diffusion de documents scientifiques de niveau recherche, publiés ou non, émanant des établissements d'enseignement et de recherche français ou étrangers, des laboratoires publics ou privés.



Distributed under a Creative Commons CC BY 4.0 - Attribution - International License

Spin-valley coupling enhanced high- T_C ferromagnetism in a non-van der Waals monolayer Cr_2Se_3 on graphene

Received: 1 October 2023

Accepted: 28 March 2025

Published online: 18 April 2025

Check for updates

C.-W. Chuang¹✉, T. Kawakami¹, K. Sugawara^{1,2,3}, K. Nakayama¹, S. Souma^{2,4}, M. Kitamura^{5,6}, K. Amemiya⁵, K. Horiba⁶, H. Kumigashira⁷, G. Kremer⁸, Y. Fagot-Revurat⁸, D. Malterre⁸, C. Bigi⁹, F. Bertran⁹, F. H. Chang¹⁰, H. J. Lin¹⁰, C. T. Chen¹⁰, T. Takahashi¹, A. Chainani¹⁰✉ & T. Sato^{1,2,4,11,12}✉

Spin-valley magnetic ordering is restricted to layered van der Waals type transition-metal dichalcogenides with ordering temperatures below 55 K. Recent theoretical studies on non-van der Waals structures have predicted spin-valley polarization induced semiconducting ferromagnetic ground states, but experimental validation is missing. We report high-Curie temperature ($T_C \sim 225$ K) metallic ferromagnetism with spontaneous spin-valley polarization in monolayer Cr_2Se_3 on graphene. Angle-resolved photoemission spectroscopy (ARPES) reveals systematic temperature-dependent energy shifts and splitting of localized Cr $3d^{\uparrow}t_{2g}$ bands, accompanied by occupancy of the itinerant Cr $3d-e_g$ valleys. The $t_{2g}-e_g$ spin-valley coupling at the K/K' points of hexagonal Brillouin zone leads to ferromagnetic ordering. Circular dichroism in ARPES shows clear evidence of spin-valley polarized states. Comparison with bilayer and trilayer Cr_2Se_3 reveals the crucial role of valley carrier density in enhancing T_C and provides a guiding principle to realize 2D ferromagnetism at higher temperatures in non-van der Waals materials.

Low-dimensional transition-metal (TM) chalcogenides continue to attract enormous attention due to the large variety of their exotic properties^{1,2}. While charge-density waves and superconductivity^{3,4} were reported in quasi-one-dimensional (1D) TM-trichalcogenides and quasi-two-dimensional (2D) TMDs (dichalcogenides) more than 50 years ago, recent discoveries include quantum anomalous Hall effect⁵, valley polarization^{6,7}, skyrmionics^{8,9} behavior, long-range magnetic order in

anisotropic 2D chalcogenides^{10,11}. Since magnetism in 2D materials or the so-called van der Waals magnets^{10,11} is forbidden in the 2D isotropic Heisenberg model by the Mermin-Wagner theorem¹², it was rationalized on the basis of anisotropy in the few-layer or monolayer (ML) limit. Further studies showed that the 2D magnets could be manipulated by variation of thickness^{13–15}, electrostatic doping^{16,17}, and/or strain^{18,19}, thus making them the primary choice for next-generation spintronic devices,

¹Department of Physics, Graduate School of Science, Tohoku University, Sendai 980-8578, Japan. ²Advanced Institute for Materials Research (WPI-AIMR), Tohoku University, Sendai 980-8577, Japan. ³Precursory Research for Embryonic Science and Technology (PRESTO), Japan Science and Technology Agency (JST), Tokyo 102-0076, Japan. ⁴Center for Science and Innovative in Spintronics (CSIS), Tohoku University, Sendai 980-8577, Japan. ⁵Institute of Materials Structure Science, High Energy Accelerator Research Organization (KEK), Tsukuba, Ibaraki 305-0801, Japan. ⁶National Institutes for Quantum Science and Technology (QST), Sendai 980-8579, Japan. ⁷Institute of Multidisciplinary Research for Advanced Materials (IMRAM), Tohoku University, Sendai 980-8577, Japan. ⁸Institut Jean Lamour, UMR 7198, CNRS, Université de Lorraine, F-54000 Nancy, France. ⁹Synchrotron SOLEIL, L'Orme des Merisiers, Départementale 128, 91190 Saint-Aubin, France. ¹⁰National Synchrotron Radiation Research Center, Hsinchu 30077, Taiwan ROC. ¹¹International Center for Synchrotron Radiation Innovation Smart (SRIS), Tohoku University, Sendai 980-8577, Japan. ¹²Mathematical Science Center for Co-creative Society (MathCCS), Tohoku University, Sendai 980-8577, Japan. ✉e-mail: chien-wen@arpes.phys.tohoku.ac.jp; chainani.ash@nsrrc.org.tw; t-sato@arpes.phys.tohoku.ac.jp

such as magnetic tunnel junctions, spin-valves, and spin-orbital torque devices^{20–22}.

Several important studies on the van der Waals magnets, namely $\text{Cr}_2\text{Ge}_2\text{Te}_6$ ¹³, CrI_3 ¹⁴, and Fe_3GeTe_2 ^{15,16}, have indicated a seemingly universal trend of a decrease in the ferromagnetic (FM) T_C on reducing thickness. However, there are conflicting reports in the Cr-Te system: while a study of single crystal films of Cr_2Te_3 /mica reported an increase in T_C from 160 K (for a thick 40.3 nm film) to $T_C = 280$ K (for a 4 unit cell, 5.5 nm film)²³, a very recent study showed a reduction in T_C from $T_C = 170$ K for 3 ML and 6 ML films to $T_C = 90$ K for a ML²⁴. On the other hand, bulk Cr_2S_3 and Cr_2Se_3 showing the same rhombohedral ($R\bar{3}$, No. 148) crystal structure exhibit antiferromagnetic (AF) order with $T_N = 120$ K²⁵ and -45 K²⁶, respectively. While ML Cr_2S_3 shows a very weak ferrimagnetic onset with $T_N = 120$ K²⁷, surprisingly, ML Cr_2Se_3 shows AF order when it is grown on Al_2O_3 ($T_N = 40$ K)²⁸ or SiO_2/Si ($T_N = 28$ K)²⁹, but on HOPG (Highly oriented pyrolytic graphite), it becomes a FM metal with $T_C = 200$ K³⁰. This is rather puzzling, and as yet, there is no clear understanding of what makes ML Cr_2Se_3 an AF insulator when it is grown on semiconducting or insulating substrates, but shows FM order on a HOPG substrate.

Another very important issue regarding ML Cr_2Se_3 is the role of inequivalent valley states providing valley degrees of freedom at the K and K' points in its band structure. A recent first-principles calculation showed that a combination of broken inversion symmetry, strong spin-orbit coupling (SOC), and magnetic exchange interaction with intrinsic out of plane magnetization in ML Cr_2Se_3 result in a spontaneous coupling of spin and valley polarization, leading to a FM semiconductor with anomalous valley Hall effect³¹. However, to date, there is no experimental report of spin-valley coupling in bulk or ML Cr_2Se_3 , or for that matter, in any non-van der Waals material. In fact, spin-valley coupling with magnetic order has been theoretically predicted in other structures^{32,33} but it has been observed only in van der Waals type materials such as WSe_2 , NbSe_2 , or their heterostructures in combination with 2D topological insulators or magnets^{34–36}. Furthermore, to date, there is no experimental evidence of FM/AF ordering temperatures getting enhanced or larger than 55 K³⁷ due to spin-valley coupling.

In this work, we have carried out a careful study of well characterized ML, 2 ML, and trilayer (3 ML) films of Cr_2Se_3 /graphene. Cr_2Se_3 is a non-van der Waals material and its thinnest limit (defined as ML with one unit cell thickness) consists of a quintuple Se-Cr-Se-Cr-Se atomic layers (see Fig. 1a for the crystal structure). We identify the localized spin as well as the itinerant valley electronic states, and then explore the relation of spin-valley coupling with FM order as a function of thickness by angle-resolved photoemission spectroscopy (ARPES).

Results and discussion

Fabrication and characterization of ML Cr_2Se_3

First, we present fabrication and characterization of a ML Cr_2Se_3 film. Since Cr chalcogenides are stabilized with a few different chemical compositions such as CrSe_2 (12 phase)^{38,39} and Cr_2Se_3 (23 phase)²⁶, it is important to identify the 23-phase nature of our film. The reflection high-energy electron diffraction (RHEED) pattern of the fabricated film shows clear streaks associated with the 1×1 structure of Cr_2Se_3 , besides the 1×1 pattern from 2 ML graphene (Fig. 1b). The estimated in-plane lattice constant (3.6 Å) is close to the value (3.62 Å) from the first-principles calculations³¹ and supports the formation of the 23 phase, as directly confirmed by the transmission electron microscopy (TEM) measurements (for details, see Figs. S1–S3 in Supplementary Note 1). Low-energy electron diffraction (LEED) pattern shows sharp six-fold 1×1 spots originating from the Cr_2Se_3 film besides the 1×1 spots of graphene (Fig. 1c), indicative of its high single crystallinity. The clear observation of graphene spots in RHEED and LEED patterns is a signature of ML formation, as reported in TMDs^{40–42}. Soft X-ray (SX)

photoemission spectroscopy shows Cr^{3+} features and supports the formation of the 23 phase (for details, see Fig. S4 of Supplementary Note 2). To clarify possible ferromagnetism, we carried out x-ray absorption spectroscopy (XAS) and magnetic circular dichroism (XMCD) at the Cr L edge ($2p\text{-}3d$ transition). The XAS spectrum at $T = 70$ K for both positive and negative out-of-plane magnetic field (± 1.0 T) shown in Fig. 1d is characterized by the Cr L_3 and L_2 main peaks at $h\nu = 577$ eV and 585 eV, respectively. The XAS spectra show a small but finite difference between the $+1.0$ T and -1.0 T, signifying a finite XMCD signal indicative of ferromagnetism. This is better visualized by the difference spectrum plotted on an expanded y-scale (green area) in which the overall XMCD spectral shape is consistent with that of ML Cr_2Se_3 and Cr_2Te_3 ^{30,43,44}. Cluster model calculations are consistent with experiments (Fig. 1d) and indicate that ML Cr_2Se_3 is a negative-charge transfer material with $\text{Cr}^{3+} t_{2g}^{3\uparrow}$ configuration and a magnetic moment of $3.4 \mu_B/\text{Cr-atom}$ (for details, see Supplementary Note 3). These results suggest that the 2D magnetism is realized in a non-van der Waals material. Since non-van der Waals 2D materials in the ultrathin limit cannot be easily obtained by a simple mechanical exfoliation of bulk crystal, the present result indicates the importance of molecular-beam epitaxy (MBE) for realizing properties unique to non-van der Waals 2D epitaxial films. One also expects a stronger interfacial effect with other materials due to the absence of a van der Waals gap, which would be useful for modulating or enhancing the magnetic properties.

To clarify the electronic states relevant to the occurrence of ferromagnetism, we investigated the band structure in the FM phase. Energy distribution curves (EDCs) measured along the ΓK cut of the hexagonal Brillouin zone (inset) in Fig. 1e signify highly dispersive valence bands located at the binding energy (E_B) of 1–3 eV, whereas the intensity within the E_B range of 0–1 eV is suppressed due to the band-gap opening. A careful look in close vicinity of E_F around the K point reveals the existence of a Fermi-edge cut-off indicative of the metallic nature. This is due to the appearance of an electron pocket as seen in the magnified EDCs and corresponding intensity plots (insets of Fig. 1e, f). The overall valence-band structure is better visualized by the ARPES-intensity plot as a function of k_y and E_B in Fig. 1f which displays the complex band structure characterized by several holelike bands centered at the Γ point and an M-shaped band around $E_B = -2$ – -2.5 eV. From the energy separation between the top of valence bands at the Γ point and the bottom of conduction bands at the K point, it is suggested that ML Cr_2Se_3 is a semiconductor in non-doped regime with an indirect band gap of ~ 0.8 eV. As shown by a side-by-side comparison of Fig. 1f, g, the overall band structure determined by ARPES shows a qualitative agreement with the calculated band structure for free-standing ML Cr_2Se_3 obtained from first-principles calculations for the FM phase assuming out-of-plane magnetic moments and an on-site Coulomb energy of $U = 3.5$ eV³¹. For example, the experimental holelike band topped at the Γ point shows a good correspondence to the top of calculated up-spin bands (red curves), and the M-shaped down-spin bands (blue curves) are commonly recognized at -1 eV below the valence-band top, in both the experiment and calculation. The momentum location (the K point) of the bottom of the conduction band which is assigned to the up-spin Cr $3d e_g^\uparrow$ band is also well reproduced by the calculation although the calculation underestimates the band-gap magnitude by $\sim 30\%$. The appearance of the e_g^\uparrow electron pocket suggests that ML Cr_2Se_3 grown on 2 ML graphene is a doped semiconductor with half-metallic nature. To identify the orbital character of observed bands, we carried out resonant ARPES measurements using SX photons around the Cr L_3 absorption edge (for details, see Fig. S5 of Supplementary Note 4). The results show a strong resonance enhancement of ARPES intensities at $E_B = -1.5$ – -2.5 eV associated with the Cr $3d\text{-}t_{2g}^\uparrow$ bands hybridized with the Se $4p$ states (for details of the orbital assignments, see Supplementary Note 5).

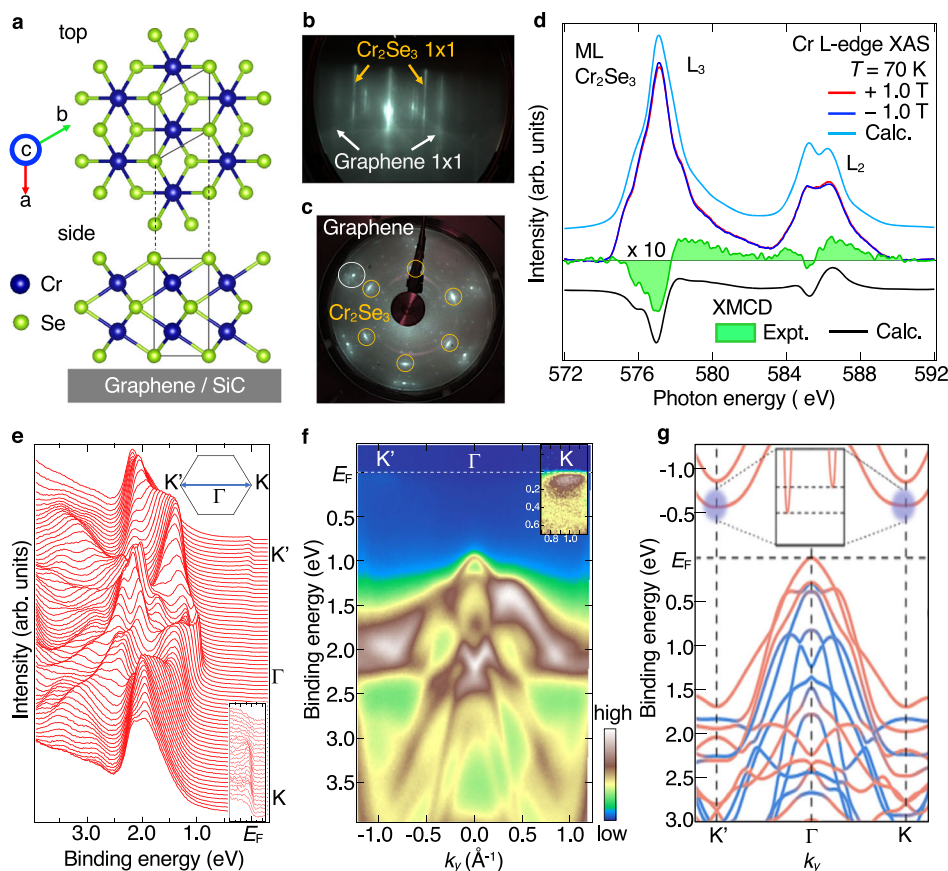


Fig. 1 | Fabrication and characterization of ML Cr_2Se_3 film. **a** Top and side views of crystal structure ($P6-m2$ space group) of ML Cr_2Se_3 on 2 ML graphene/SiC (0001). Black rectangles show the unit cell which consists of quintuple layers with Se-Cr-Se-Cr-Se stacking sequence. **b** RHEED pattern of ML Cr_2Se_3 . White and yellow arrows indicate the 1×1 patterns from graphene and Cr_2Se_3 , respectively. **c** LEED pattern of ML Cr_2Se_3 measured with the primary electron energy of 90 eV. Yellow and white circles represent the 1×1 spots from Cr_2Se_3 and graphene, respectively. **d** Cr L edge ($2p-3d$) XAS spectrum of ML Cr_2Se_3 measured with applied magnetic field of ± 1.0 Tesla (T) at 70 K (red and blue curves). Green area shows the subtraction between $+1.0$ T and -1.0 T data expanded vertically by 10 times, corresponding to the experimental XMCD. Numerical simulation based on the charge

transfer cluster model for XAS and XMCD spectra are displayed with light blue and black curves, respectively. **e**, **f** EDCs and corresponding ARPES intensity plot as a function of k_y and E_B , respectively, measured along the Γ K cut at $T = 40$ K with circularly polarized light of $h\nu = 75$ eV. Insets show the expanded EDCs and the ARPES intensity with enhanced color contrast around the K point. **g** Calculated band structure for free-standing ML Cr_2Se_3 (ref. 31) which takes into account the SOC and assumes the out-of-plane magnetization. Spin-up and spin-down bands are shown by red and blue curves, respectively. Inset shows the expansion of the conduction-band bottom which signifies the energy difference of 18 meV between two inequivalent K points³¹. Panel **g** reproduced with permission from ref. 31, American Physical Society.

Temperature dependence of the band structure across T_C

Now that the overall band structure in the FM phase is established, next we show temperature evolution of the band structure in Fig. 2a–c (detailed T -dependence is shown in Fig. S13). Key characteristics of the complex band structure seen at $T = 40$ K in Figs. 1f, 2a, such as the M-shaped band around $E_B - 2-2.5$ eV and a sharp valence-band top at the Γ point, still persist at $T = 150$ K (Fig. 2b). In contrast, at $T = 300$ K (Fig. 2c), the spectral feature becomes simpler and the M-shaped band is converted to a V-shaped band located around $E_B - 1.3-2.1$ eV. As shown later, the detailed analysis and temperature-dependent XMCD measurements suggest that T_C lies between 225 and 250 K, higher than the estimated T_C value of ~ 200 K in ML Cr_2Se_3 on HOPG³⁰.

Besides a drastic change in the band structure, a systematic T -dependent energy shift is observed in the EDCs and corresponding second-derivative intensity plots at the Γ point ($k_y = 0.0 \text{ \AA}^{-1}$) in Fig. 2d, g. All the bands, including the topmost valence band and corresponding spin-orbit split Se $4p$ states separated by -0.2 eV^{45} , systematically move toward E_F on increasing temperature upto T_C , with a gradual increase in the peak width associated with thermal broadening. This is also the case for the spectra at the K' point ($k_y = -1.1 \text{ \AA}^{-1}$; Fig. 2e, h). Besides the systematic band shift, some bands show additional energy splitting at low temperatures. For example, at the Γ point (Fig. 2d), a main peak at

$E_B = 2.16 \text{ eV}$ with a shoulder feature at 2.36 eV at $T = 40 \text{ K}$, signify the existence of a double peak (marked as p1 and p2 in Fig. 2d). This double peak consisting of Cr-Se hybridized states constituting the M-shaped band get merged into a single peak on increasing temperature, around $T = 225-250 \text{ K}$. We quantified the T -dependence of band energies from numerical fits to the EDCs and the peak positions are shown in Fig. 2f. The band splitting vanishes between $T = 225-250 \text{ K}$, corresponding to T_C of ML Cr_2Se_3 . The same trend is also recognized for the peaks at -1.97 eV and -2.13 eV at $T = 40 \text{ K}$ for the K' point (Fig. 2e, h) and corresponding plots of the t_{2g} band energies in Fig. S7c (for details, see Supplementary Note 6). We attribute the above observation to the band splitting associated with the FM transition, since the splitting sets in around T_C , as is also confirmed by the T -dependent XMCD signal shown in Fig. S18. Such a clear T -dependent band splitting below T_C has been rarely reported in 2D ferromagnets^{24,46}.

Spin-valley coupling

We found a signature of circular dichroism (CD) for the t_{2g}^\uparrow bands at the K and K' points at $T = 40 \text{ K}$ for ML Cr_2Se_3 , as shown Fig. 2i. Using right and left circularly polarized light (C^+ and C^-), the obtained EDCs at the K point (red and pink curves) show a difference between their peak intensities, signifying a finite CD. This CD is also observed at the K'

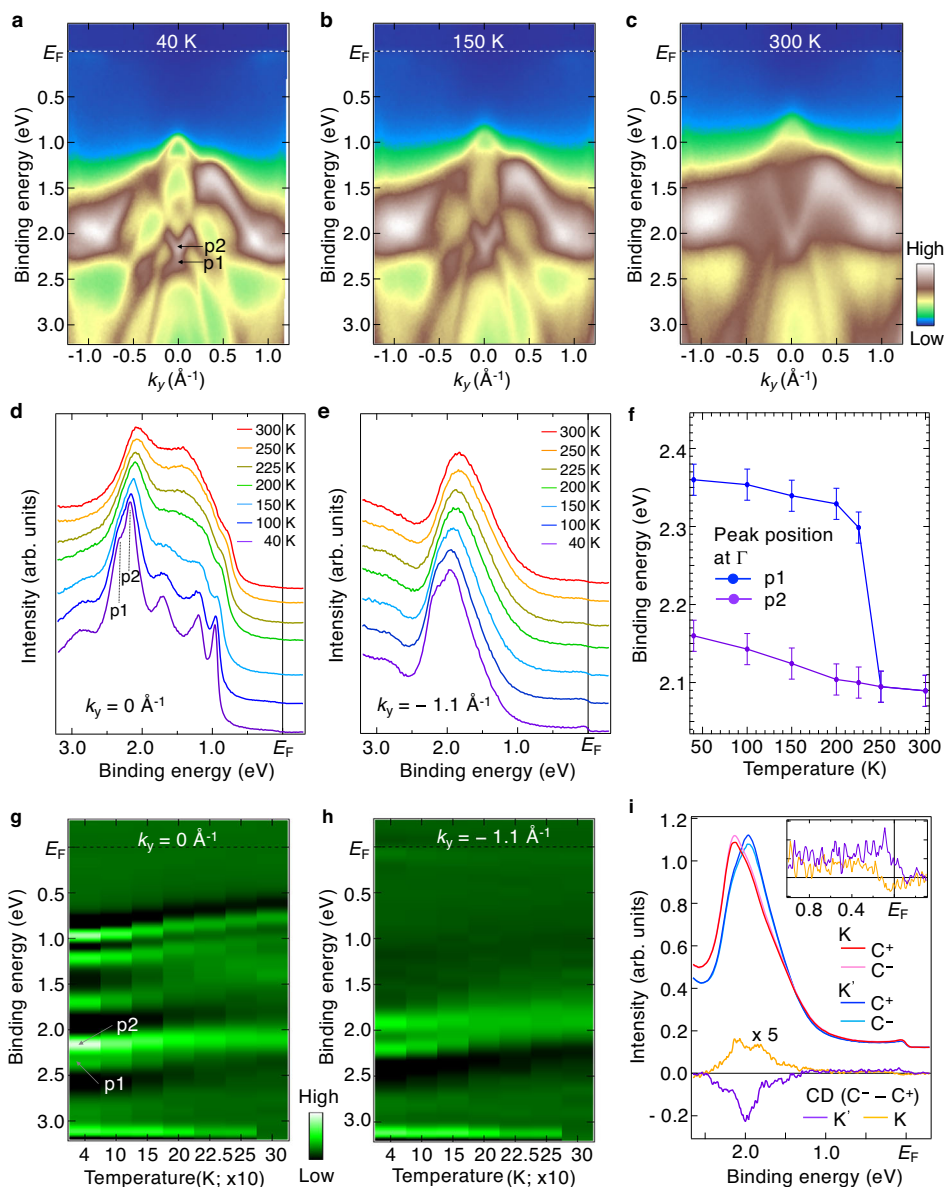


Fig. 2 | Temperature evolution of band structure and evidence for spin-valley polarization. **a–c** ARPES-intensity plots along the Γ K cut measured at $T = 40$ K, 150 K, and 300 K, respectively, measured with circularly polarized photons of $h\nu = 75$ eV. Peaks p1 and p2 are also indicated. **d, e** Temperature-dependence of EDCs at selected k cuts at $k_y = 0.0$ (Γ), -1.1 \AA^{-1} (K'), respectively. **f** Temperature dependence of the peak position for valence-band peaks at $E_B - 2 - 2.5$ eV at the Γ point ($k_y = 0 \text{ \AA}^{-1}$) estimated by numerical fittings to the EDCs assuming Voigt peaks

and linear background with error bars ± 20 meV. **g, h** Second-derivative intensity plots of Fig. 2d, e, respectively. **i** EDCs for ML Cr_2Se_3 , obtained at the K and K' points with C^+ and C^- polarized lights using $h\nu = 75$ eV. Yellow and purple curves represent subtracted EDCs obtained with C^+ and C^- photons expanded vertically by 5 times. Inset shows the expansion near E_F . One can recognize a clear circular dichroism (CD) associated with spin-valley polarization which reverses its sign between the K and K' points.

point (blue and light blue curves) but with a sign reversal compared to the K point, as shown by the subtracted EDCs expanded vertically (yellow and purple curves). We found a sign reversal of CD also for the e_g^\uparrow pocket between the K and K' points (see inset to Fig. 2i). Intriguingly, the sign is also reversed between the t_{2g}^\uparrow and e_g^\uparrow bands. These observations suggest that photoelectron excitations are asymmetric between the K and K' points, supporting the valley-selective CD (i.e., valley polarization) which is a necessary condition for realizing anomalous valley Hall effect³¹. It is noted that the observed CD is not likely to originate from experimental artifacts such as incomplete CD polarization or sample degradation, but is an intrinsic property of our Cr_2Se_3 film (for details, see Supplementary Note 7). This is also corroborated by the observation of three-fold symmetric LEED pattern suggestive of the inequivalently mixed structure domains rotated by 60° from each other (in this regard, it is different from ML 1T' TMDs

with equivalently mixed 120° rotated domains^{47–50}), making our Cr_2Se_3 film a valid candidate to observe valley polarization (for details, see Fig. S8 and Supplementary Note 7).

We found that the overall magnitude of CD is reduced in the 2 ML sample with lower T_C (see Fig. S9 in Supplementary Note 7), signifying that the valley-selective CD is coupled to the ferromagnetism. This coupling of localized t_{2g} -spins and itinerant e_g -valley states is supported by considering the magnitude of experimental energy splitting for the strongly hybridized t_{2g} bands at the K/ K' point for ML (~ 160 meV) which is much larger than the SOC energy (Δ_{SOC}) of Cr^{3+} states (~ 50 meV) and inversion-symmetry breaking of the crystal (at most a few tens meV)³¹. But the observed splitting is comparable to the known Δ_{SOC} of ~ 200 meV in Se bands⁴⁵, which is about half of the atomic SOC energy $\Delta'_{\text{SOC}} = 418$ meV for Se $4p$ states. In a recent study on $\text{V}_{1/3}\text{NbS}_2$ crystals, a giant valley-Zeeman coupling in surface states of

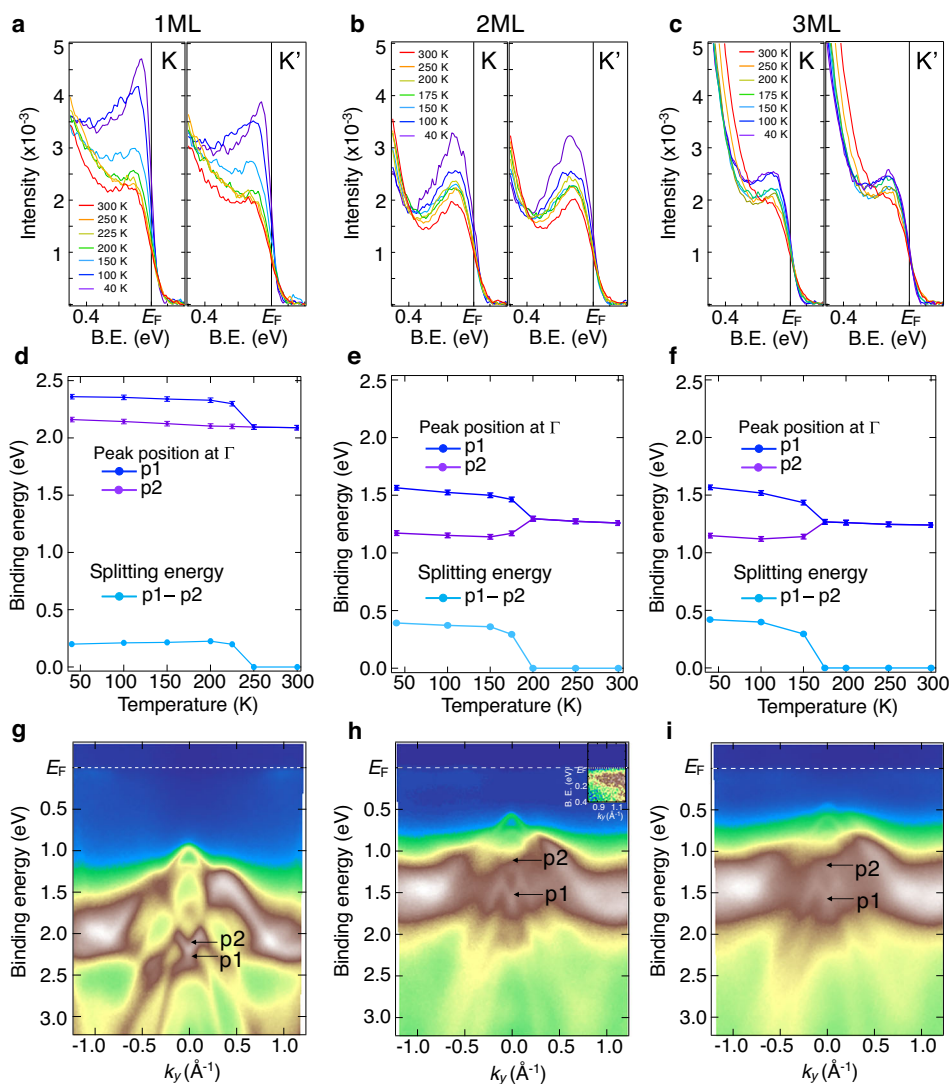


Fig. 3 | Thickness dependence of electronic states. **a–c** Temperature dependence of EDCs near E_F at the K ($k_y = 1.1 \text{ \AA}^{-1}$; left panel) and K' ($k_y = -1.1 \text{ \AA}^{-1}$; right panel) points to the evolution of the e_g^\uparrow electron pocket for ML Cr_2Se_3 . The spectral weight is normalized to the valence-band t_{2g} peak. **d–f** Temperature dependence of the peak position for valence-band peaks p1 and p2 at the Γ point estimated by numerical fittings to the EDCs for ML, 2 ML, and 3 ML Cr_2Se_3 , respectively, suggesting the

gradual reduction of T_C upon increasing the number of layers n . **g–i** ARPES-intensity plots as a function of k_y and E_B along the Γ K cut measured with $h\nu = 75 \text{ eV}$ photons at $T = 40 \text{ K}$ for ML, 2 ML, and 3 ML Cr_2Se_3 , respectively. Inset to **(h)** shows the ARPES intensity with enhanced color contrast around the K point. B. E. stands for binding energy.

the NbS_2 -termination top layer was reported to originate from hybridized Vd orbitals and planar NbS_2 orbitals with an exchange splitting $\Delta_{\text{ex}} \sim 52 \text{ meV}$ and $\Delta_{\text{SOC}} \sim 59 \text{ meV}$ aiding each other at the K point and opposing each other at the K' point. Using known values of valley-Zeeman splitting of -0.2 meV T^{-1} for TMDs⁵¹, the authors estimated that a magnetic field exceeding 250 T was operative in $\text{V}_{1/3}\text{NbS}_2$ to give the observed splitting. However, the results showed that the surface states of $\text{V}_{1/3}\text{NbS}_2$ exhibit the same magnetic ordering temperature as the bulk, with $T_N \sim 53 \text{ K}$ ³⁷. In the present case, we see ferromagnetism with a relatively high $T_C \sim 225 \text{ K}$ for ML Cr_2Se_3 case compared to an antiferromagnetic $T_N \sim 45 \text{ K}$ for bulk Cr_2Se_3 ²⁶. However, we see an experimental energy splitting for the t_{2g} bands at the K/K' point for ML ($\sim 160 \text{ meV}$) suggesting a spin-splitting-dominated spin-valley coupling since the valley splitting is calculated to be just 18 meV ³¹. Moreover, the gradual reduction of the splitting energy with a small reduction in T_C by increasing number of layers (see Fig. S7 in Supplementary Note 6) also supports the intimate coupling of spin and valley degrees of freedom for an enhanced T_C in 2 ML and 3 ML films compared to bulk $T_N \sim 45 \text{ K}$.

Besides the spin-valley coupling, another intriguing characteristic of ML Cr_2Se_3 is the evolution of the e_g^\uparrow electron pocket at the K/K' point. The EDCs in Fig. 3a signify a sharp peak associated with the e_g^\uparrow band at $T = 40 \text{ K}$ for both the K and K' points. Upon increasing temperature, the spectral weight of e_g^\uparrow -peak is monotonically reduced and the peak has almost vanished at $T = 300 \text{ K}$. This suggests that ferromagnetism in ML Cr_2Se_3 is associated with spectral weight of the e_g^\uparrow pocket. Figure 3a shows that the total spectral weight at fixed temperature is higher at the K point than at the K' point (see purple or blue curves). This intensity asymmetry is attributed to the inequivalent valley states at the K and K' points predicted by the density-functional-theory (DFT) calculation³¹ and associated with the spin-valley coupling. We have carefully examined this inequivalent valley states between the K and K' points, and found that the asymmetric nature is reproducible for different samples. More intriguingly, the asymmetry gets enhanced after applying out-of-plane magnetic field, supporting the spin-valley coupling (for details, see Figs. S10 and S11 in Supplementary Note 8).

In particular, ARPES measurements on ML Cr_2Se_3 film with improved statistics were carried out to confirm the inequivalence of

valley states at K and K' points. ARPES intensity maps around the K' and K points, obtained after normalizing the total spectral weight over the plotted E_B range of E_F to 2.7 eV (Fig. S10a, b) indicate that the intensity of the electron pocket around the K point is higher than that around the K' point, confirming the inequivalent valley states around K and K'. Overlapped EDCs at positive k_y 's and negative k_y 's (Fig. S10c) clearly indicate that the spectral weight of the e_g^- -derived peak for positive k_y 's is higher than that for negative k_y 's.

To clarify the possible coupling of inequivalent valley states to the spin degrees of freedom, we performed ARPES measurements after magnetizing the sample by applying an out-of-plane magnetic field with the strength of $\mathbf{B} = +0.1$ T (see EDCs in Fig. S10d). While the overall spectral intensity of the electron pocket is slightly reduced, the asymmetric intensity of the EDCs between the K and K' points indicate that the inequivalence is preserved even after applying \mathbf{B} . To our surprise, we found that a broad shoulder feature appears at $E_B - 0.2$ eV more prominently for negative k_y 's, i.e., around the K' point, suggesting that the shape of the EDCs becomes more inequivalent after applying \mathbf{B} . This change is highlighted by a direct comparison of EDCs at the K and K' points (Fig. S11a, b) indicating that the spectral weight of the shoulder feature is enhanced at the K' point after applying \mathbf{B} , which is also confirmed by our numerical analysis of EDCs (Fig. S12). We found that the shoulder feature becomes much weaker and the EDC shows a simpler peak shape at the K' point upon reversing \mathbf{B} , becoming similar to the spectrum at the K point obtained by applying positive \mathbf{B} (Fig. S11c). In addition, we confirmed that this result is reproducible for different samples, by measuring another ML Cr_2Se_3 sample (Fig. S11d). This finding strengthens our argument on the observation of inequivalent valley states between the K and K' points and their coupling to the spontaneous ferromagnetism.

Band structure of multilayer Cr_2Se_3

Next, we fabricated 2 ML and 3 ML Cr_2Se_3 films to investigate thickness evolution of their band structure and relation with spin-valley states. We found that the energy bands of 2 ML and 3 ML films (Fig. 3h, i) are shifted upward by -0.4 and -0.5 eV, respectively, compared to the ML film (Fig. 3g). Simultaneously, the Cr $3d$ t_{2g} bands get significantly broadened, and also show larger band splitting at the Γ point. Detailed analysis at the Γ point (and the K point; see Fig. S7 in Supplementary Note 6) shown in Fig. 3d–f suggests that the T_C gradually decreases on increasing the number of layers n ; $T_C = 225$ –250 K, 175–200 K, and 150–175 K, for ML, 2 ML, and 3 ML, respectively (for detailed T -dependent ARPES data and quantitative analyses of the band splitting, see Figs. S13–17 in Supplementary Note 9). We have confirmed that T_C 's estimated by ARPES and XMCD well coincide with each other, suggesting the validity of the T_C estimation from the band splitting (for details, see Fig. S18 in Supplementary Note 10). The T_C reduction is correlated with the spectral weight at E_F of metallic e_g^+ pocket seen for ML (Fig. 3a), which gets reduced in 2 ML (Fig. 3b) and almost vanishes in 3 ML (Fig. 3c) (note that a tiny electron pocket still exists at low temperatures for 2 ML, as seen in the image with enhanced color contrast in the inset to Fig. 3h). This is consistent with the observed valence-band shifts on increasing n and indicates that the highest doping of electron carriers occurs in the ML film at low- T . It is noted that the asymmetric intensity distribution of the e_g^+ band between the K and K' points observed for ML gets reduced for 2 ML and 3 ML (Fig. 3b, c), confirming the coupling of valley anisotropy and ferromagnetism. Interestingly, a very recent study²⁴ on Cr_2Te_3 showed that 3 ML and 6 ML films with $T_C = 170$ K and T -dependent band shifts, exhibit a reduced $T_C = 90$ K in ML with no energy band shifts, indicating a Stoner to Heisenberg (itinerant to localized)-type FM order. In contrast, Cr_2Se_3 shows an enhancement of T_C in the ML case with $T_C = 225$ K compared to 2 ML ($T_C = 175$ K) and 3 ML films ($T_C = 150$ K), derived from spin-valley coupling of localized and itinerant states.

The most reasonable explanation of the observed n -dependent band structure and FM T_C 's is the charge transfer from the graphene substrate^{39,52}, which is also supported by directly comparing the binding energy of the Dirac point of graphene bands before and after the fabrication of ML Cr_2Se_3 (for details, see Fig. S19 in Supplementary Note 11). Accordingly, the doped electron carrier density per unit Cr_2Se_3 layer is expected to be reduced for multilayer films since the total amount of transferred charge carriers across the interface is fixed; this behavior is realized in the present study. Since the Mermin-Wagner theorem¹² suggests that FM order is suppressed upon reducing n , in contrast to present observations, the enhancement of T_C up to 225–250 K in ML is likely due to the RKKY mechanism associated with maximum carrier density in e_g^+ valley states. This argument also explains why the insulating ML Cr_2Se_3 films fabricated on Al_2O_3 or SiO_2/Si do not show FM but AF order, as in the bulk crystal^{26,28,29}, because no charge transfer is expected from insulating Al_2O_3 or SiO_2/Si in contrast to the present study which uses a metallic 2 ML graphene/ SiC substrate. It also explains the observation of high- T_C ferromagnetism ($T_C = 200$ K) for ML Cr_2Se_3 on HOPG³⁰, comparable to the present work because charge-transfer characteristics of graphene and HOPG are expected to be similar with nearly equal work functions.

Finally, we discuss important differences between Cr_2Se_3 and Cr-Te based van der Waals ferromagnets $\text{Cr}_2\text{Ge}_2\text{Te}_6$ and CrTe_2 . A critical difference is that tellurium compounds commonly show ferromagnetism in the bulk whereas bulk Cr_2Se_3 is an anti-ferromagnetic ($T_N = 45$ K) semiconductor. Moreover, only Cr_2Se_3 transforms into a ferromagnetic metal with $T_C = 225$ K for ML films grown on graphene ($T_C = 200$ K for ML $\text{Cr}_2\text{Se}_3/\text{HOPG}$; ref. 30). In contrast, the van der Waals ferromagnets, namely $\text{Cr}_2\text{Ge}_2\text{Te}_6$ (ref. 13) and CrTe_2 show a reduction in T_C on decreasing thickness (although there are conflicting reports for Cr_2Te_3 as discussed above^{23,24}). Reference²⁴ showed that the dominantly Te character orbitals cross E_F in Cr_2Te_3 and form the Fermi surface, leading to an itinerant Stoner type ferromagnetism in thick Cr_2Te_3 films, but for ML Cr_2Te_3 film, the Stoner condition is not satisfied and a local moment Heisenberg exchange driven ferromagnetism is realized. In contrast, the Se bands in Cr_2Se_3 sink well below E_F and the occupation of the valley electron pockets with Cr $3d$ e_g character, which couple with localized t_{2g} spins, promotes the ferromagnetism. These aspects suggest that the origin of ferromagnetism in Cr_2Se_3 films on graphene or HOPG can be expected to be qualitatively different from the van der Waals ferromagnets (it is noted here that, in the ML limit, Cr_2Te_3 suffers from a trigonal distortion²⁴ with a 2×2 superstructure whereas Cr_2Se_3 maintains its 1×1 structure, which can lead to differences in their magnetic properties). Also, the double exchange mechanism is usually considered for the case of mixed valent materials, which is unlikely for Cr_2Se_3 films on graphene, distinct from the situation of $\text{Cr}_2\text{Ge}_2\text{Te}_6$ (refs. 53,54); for a detailed discussion, see Supplementary Note 12. Our results in Fig. 3, corroborated by temperature-dependent XMCD, suggest that the reduction of T_C on increasing the number of layers is caused by a reduction in the electron carrier density transferred from the substrate across the interface. The results taken together indicate that the T_C is proportional to the carrier density (this is supported by the plot of T_C vs spectral density of states at E_F in Fig. S20), and hence suggest that the ferromagnetism is likely due to the localized t_{2g} spins coupled by the RKKY interaction active in the valley electron pockets of Cr_2Se_3 films grown on graphene.

Methods

Fabrication of ML Cr_2Se_3

We fabricated monolayer (ML) Cr_2Se_3 on bilayer (2 ML) graphene grown on an n -type 6H-SiC (0001) substrate using molecule-beam-epitaxy (MBE) method. We have selected graphene as a substrate by

taking account of the symmetry matching with Cr₂Se₃, 2 ML graphene was grown by resistive heating of an *n*-type 6H-SiC (0001) substrate at 1120 °C for 30 minutes in an ultrahigh vacuum (UHV) of 5×10^{-9} Torr. Then, we fabricated ML Cr₂Se₃ on 2 ML graphene/6H-SiC (0001) by evaporating Cr atoms in Se atmosphere. The substrate temperature was kept at 300 °C during the epitaxy. The fabricated film was then annealed at 300 °C for 30 min. to improve the crystal quality. To monitor the sample growth, we used the reflection high-energy electron diffraction (RHEED). Low-energy electron diffraction (LEED) was also carried out to confirm the absence of surface reconstruction. We have also carried out high-angle annular dark-field TEM measurements for Se-capped ML Cr₂Se₃ film to confirm the growth of the Cr₂Se₃ phase.

XAS and XMCD measurements

The Cr L-edge (*2p-3d*) X-ray absorption spectroscopy (XAS) and X-ray magnetic circular dichroism (XMCD) of ML Cr₂Se₃ were performed at the beamline of BL-16A in KEK-PF (Photon factory). X-ray photons with right (C⁺) or left (C⁻) circular polarization with normal incidence to the sample surface were introduced into the measurement chamber. The external magnetic field (**B**) of ± 1.0 Tesla (T) was applied normal to the sample surface. XMCD measurements were carried out by two modes, (i) switching the light polarization with fixed **B** and (ii) reversing the **B** direction with fixed light polarization. We have confirmed that both methods are consistent with each other. An XMCD spectrum for ML Cr₂Se₃ at KEK-PF was obtained under the magnetic field of ± 1.0 T by using 10-Hz circular-polarization switching at *T* = 70 K with the total electron yield mode. To eliminate an artifact associated with the experimental drift, the XMCD spectrum was obtained by averaging data measured with the above two different methods. Temperature-dependent XAS-XMCD measurements were carried out at Dragon Beamline (BL 11A) of the Taiwan Light Source by reversing the **B** direction for fixed right circular (C⁺) polarization under the magnetic field of ± 1.0 T applied normal to the sample surface. The XAS and XMCD spectra were measured using the total-electron-yield mode at selected sample temperatures between *T* = 70 K–250 K.

ARPES measurements

Since we carried out the fabrication of sample in a separate MBE chamber, we capped the fabricated ML Cr₂Se₃ film with a thin amorphous Se film in the MBE chamber to avoid the degradation during the transportation. After the sample was installed into the ARPES system in synchrotron facility, the Se film was removed by heating at 145 °C while monitoring the RHEED pattern. VUV micro-focused ARPES⁵⁵ measurements were performed at BL-28A in Photon Factory, KEK by using *hν* = 75 eV photons with circular, linearly horizontal, or linearly vertical polarization. ARPES measurements were also carried out at CASSIOPEE beamline in SOLEIL using *hν* = 50 eV photons with linearly vertical polarization. Soft X-ray and resonant ARPES measurements were carried out at BL-2A, KEK-PF with linear horizontally polarized light.

Data availability

The data that support the findings of this study are available within the main text and Supplementary Information. Any other relevant data are available from the corresponding authors upon request.

References

- Manzeli, S., Ovchinnikov, D., Pasquier, D., Yazyev, Oleg, V. & Kis, A. 2D transition metal dichalcogenides. *Nat. Rev. Mater.* **2**, 17033 (2017).
- Zhou, J. et al. A library of atomically thin metal chalcogenides. *Nature* **556**, 355–359 (2018).
- Yokoya, T. et al. Fermi surface sheet-dependent superconductivity in 2H-NbSe₂. *Science* **294**, 2518–2520 (2001).
- Morosan, E. et al. Superconductivity in Cu_xTiSe₂. *Nat. Phys.* **2**, 544–550 (2006).
- Tang, S. et al. Quantum spin Hall state in monolayer 1T'-WTe₂. *Nat. Phys.* **13**, 683–687 (2017).
- Cao, T. et al. Valley-selective circular dichroism of monolayer molybdenum disulphide. *Nat. Commun.* **3**, 887 (2012).
- Schaibley, J. et al. Valleytronics in 2D materials. *Nat. Rev. Mater.* **1**, 16055 (2016).
- Zhang, C. et al. Room-temperature magnetic skyrmions and large topological Hall effect in chromium telluride engineered by self-intercalation. *Adv. Mater.* **35**, 2205967 (2023).
- Saha, R. et al. Observation of Néel-type skyrmions in acentric self-intercalated Cr_{1+δ}Te₂. *Nat. Commun.* **13**, 3965 (2022).
- Burch, K. S., Mandrus, D. & Park, J.-G. Magnetism in two-dimensional van der Waals materials. *Nature* **563**, 47–52 (2018).
- Gong, C. & Zhang, X. Two-dimensional magnetic crystals and emergent heterostructure devices. *Science* **363**, eaav4450 (2019).
- Mermin, N. D. & Wagner, H. Absence of ferromagnetism or antiferromagnetism in one- or two-dimensional isotropic Heisenberg models. *Phys. Rev. Lett.* **17**, 1133 (1966).
- Gong, C. et al. Discovery of intrinsic ferromagnetism in two-dimensional van Der Waals crystals. *Nature* **546**, 265–269 (2017).
- Huang, B. et al. Layer-dependent ferromagnetism in a van der Waals crystal down to the monolayer limit. *Nature* **546**, 270–273 (2017).
- Fei, Z. et al. Two-dimensional itinerant ferromagnetism in atomically thin Fe₃GeTe₂. *Nat. Mater.* **17**, 778–782 (2018).
- Deng, Y. et al. Gate-tunable room-temperature ferromagnetism in two dimensional Fe₃GeTe₂. *Nature* **563**, 94–99 (2018).
- Verzhbitskiy, I. A. et al. Controlling the magnetic anisotropy in Cr₂Ge₂Te₆ by electrostatic gating. *Nat. Electron.* **3**, 460–465 (2020).
- Zhou, Y. et al. Tensile strain switched ferromagnetism in layered NbS₂ and NbSe₂. *ACS Nano* **6**, 9727–9736 (2012).
- Gebredingle, Y., Joe, M. & Lee, C. First-principles calculations of the spin-dependent electronic structure and strain tunability in 2D non-van der Waals chromium chalcogenides Cr₂X₃ (X = S, Se, Te): implications for spintronics applications. *ACS Appl. Nano Mater.* **5**, 10383–10391 (2022).
- Kim, H. H. et al. One million percent tunnel magnetoresistance in a magnetic van der Waals heterostructure. *Nano Lett.* **18**, 4885–4890 (2018).
- Wang, Z. et al. Tunneling spin valves based on Fe₃GeTe₂/hBN/Fe₃GeTe₂ van der Waals heterostructures. *Nano Lett.* **18**, 4303–4308 (2018).
- Wang, X. et al. Current-driven magnetization switching in a van der Waals ferromagnet Fe₃GeTe₂. *Sci. Adv.* **5**, eaaw8904 (2019).
- Wen, Y. et al. Tunable room-temperature ferromagnetism in two-dimensional Cr₂Te₃. *Nano. Lett.* **20**, 3130–3139 (2020).
- Zhong, Y. et al. From Stoner to local moment magnetism in atomically thin Cr₂Te₃. *Nat Commun* **14**, 5340 (2023).
- Sugiura, T., Iwahashi, K., Horai, K. & Masuda, Y. Experimental studies of rhombohedral Cr₂S₃ single crystal. I. Magnetic properties. *J. Phys. Soc. Jpn.* **38**, 365–372 (1975).
- Adachi, Y. et al. Magnetic structure of rhombohedral Cr₂Se₃. *J. Phys. Soc. Jpn.* **63**, 1548–1559 (1994).
- Chu, J. et al. Sub-millimeter-scale growth of one-unit-cell-thick ferrimagnetic Cr₂S₃ nanosheets. *Nano Lett.* **19**, 2154–2161 (2019).
- Roy, A. et al. Structural and magnetic properties of molecular beam epitaxy grown chromium selenide thin films. *Phys. Rev. Mater.* **4**, 025001 (2020).
- Zhu, X. et al. Spin glass state in chemical vapor-deposited crystalline Cr₂Se₃ nanosheets. *Chem. Mater.* **33**, 3851–3858 (2021).
- Liu, M. et al. Diverse structures and magnetic properties in non-layered monolayer chromium selenide. *J. Phys. Chem. Lett.* **12**, 7752–7760 (2021).

31. He, Z. et al. Two-dimensional valleytronic semiconductor with spontaneous spin and valley polarization in single-layer Cr_2Se_3 . *Phys. Rev. B* **104**, 075105 (2021).
32. Cui, Q., Zhu, Y., Liang, J., Cui, P. & Yang, H. Spin valley coupling in a two dimensional VSi_2N_4 monolayer. *Phys. Rev. B* **103**, 085421 (2021).
33. Zheng, G., Qu, S., Zhou, W. & Ouyang, F. Janus monolayer TaNF : a new ferrovalley material with large valley splitting and tunable magnetic properties. *Front. Phys.* **18**, 53302 (2023).
34. Zhong, D. et al. Layer-resolved magnetic proximity effect in van der Waals heterostructures. *Nat. Nanotechnol.* **15**, 187–191 (2020).
35. Matsuoka, H., Habe, T., Iwasa, Y., Koshino, M. & Nakano, M. Spontaneous spin-valley polarization in NbSe_2 at a van der Waals interface. *Nat. Commun.* **13**, 5129 (2022).
36. Bhowmik, S. et al. Spin-orbit coupling-enhanced valley ordering of malleable bands in twisted bilayer graphene on WSe_2 . *Nat. Commun.* **14**, 4055 (2023).
37. Edwards, B. et al. Giant valley-Zeeman coupling in the surface layer of an intercalated transition metal dichalcogenide. *Nat. Mater.* **22**, 459–465 (2023).
38. Freitas, D. C. et al. Antiferromagnetism and ferromagnetism in layered $1\text{T}'\text{-CrSe}_2$ with V and Ti replacements. *Phys. Rev. B* **87**, 014420 (2013).
39. Li, B. et al. Van der Waals epitaxial growth of air-stable CrSe_2 nanosheets with thickness-tunable magnetic order. *Nat. Mater.* **20**, 818–825 (2021).
40. Nakata, Y. et al. Anisotropic band splitting in monolayer NbSe_2 : implications for superconductivity and charge density wave. *Npj 2D Mater. Appl.* **2**, 12 (2018).
41. Nakamura, H. et al. Spin splitting and strain in epitaxial monolayer WSe_2 on graphene. *Phys. Rev. B* **101**, 165103 (2020).
42. Feng, J. et al. Electronic structure and enhanced charge-density wave order of monolayer VSe_2 . *Nano Lett.* **18**, 4493–4499 (2018).
43. Burn, D. M. et al. Cr_2Te_3 thin films for integration in magnetic topological insulator heterostructures. *Sci. Rep.* **9**, 10793 (2019).
44. Lee, I. H. et al. Modulating curie temperature and magnetic anisotropy in nanoscale-layered Cr_2Te_3 films: implications for room-temperature spintronics. *ACS Appl. Nano Mater.* **4**, 4810–4819 (2021).
45. Pacilé, D. et al. Photoemission and optical studies of ZrSe_3 , HfSe_3 , ZrS_3 . *Phys. Rev. B* **76**, 155406 (2007).
46. Zhang, X. et al. Room-temperature intrinsic ferromagnetism in epitaxial CrTe_2 ultrathin films. *Nat. Commun.* **12**, 2492 (2021).
47. Tang, S. et al. Quantum spin Hall state in monolayer $1\text{T}'\text{-WTe}_2$. *Nat. Phys.* **13**, 68–687 (2017).
48. Tang, S. et al. Electronic structure of monolayer $1\text{T}'\text{-MoTe}_2$ grown by molecular beam epitaxy. *APL Mater* **6**, 026601 (2018).
49. Ugeda, M. M. et al. Observation of topologically protected states at crystalline phase boundaries in single-layer WSe_2 . *Nat. Commun.* **9**, 3401 (2018).
50. Choi, B. K. Visualizing orbital content of electronic bands in anisotropic 2D semiconducting ReSe_2 . *ACS Nano* **14**, 7880–7891 (2020).
51. Srivastava, A. et al. Valley Zeeman effect in elementary optical excitations of monolayer WSe_2 . *Nat. Phys.* **11**, 141 (2015).
52. Chua, R. et al. Room temperature ferromagnetism of monolayer chromium telluride with perpendicular magnetic anisotropy. *Adv. Mater.* **33**, 2103360 (2021).
53. Trzaska, L. et al. Charge doping into spin minority states mediates doubling of T_C in ferromagnetic CrGeTe_3 . *arXiv* **2312**, 00440 (2023).
54. Wang, N. et al. Transition from ferromagnetic semiconductor to ferromagnetic metal with enhanced curie temperature in $\text{Cr}_2\text{Ge}_2\text{Te}_6$ via organic ion intercalation. *J. Am. Chem. Soc.* **141**, 17166–17173 (2019).
55. Kitamura, M. et al. Development of a versatile micro-focused angle-resolved photoemission spectroscopy system with Kirkpatrick-Baez mirror optics. *Rev. Sci. Instrum.* **93**, 033906 (2022).

Acknowledgements

This work was supported by JST-CREST (no. JPMJCR18T1), Grant-in-Aid for Scientific Research (JSPS KAKENHI Grant Number JP21H04435), KEK-PF (Proposal No. 2020G669, 2021S2-001, 2021G005, 2022PF-G005, and 2022G007), and UVSOR (Proposal No. 22IMS1205). A.C. thanks the National Science and Technology Council of Taiwan, Republic of China, for financially supporting this research under Contract Nos. NSTC 111-2112-M-213-031 and NSTC 112-2112-M-213-029. C.W.C. and T.K. acknowledge support from GP-Spin at Tohoku University and JSPS.

Author contributions

The work was planned and proceeded by discussion among C.W.C., K.S., A.C., and T.S. C.W.C. fabricated ultrathin films. C.W.C., T.K., K.S., K.N., S.S., M.K., K.A., K.H. H.K., G.K., Y.F.-R., D.M., C.B., F.B., and T.T. performed the ARPES measurements. C.W.C., K.S., F.H.C., H.J.L., C.T.C., and M.K. performed the XMCD measurements. C.W.C., A.C., and T.S. finalized the manuscript with inputs from all the authors.

Competing interests

The authors declare no competing interests.

Additional information

Supplementary information The online version contains supplementary material available at <https://doi.org/10.1038/s41467-025-58643-3>.

Correspondence and requests for materials should be addressed to C.-W. Chuang, A. Chainani or T. Sato.

Peer review information *Nature Communications* thanks Yandong Ma and the other, anonymous, reviewer(s) for their contribution to the peer review of this work. A peer review file is available.

Reprints and permissions information is available at <http://www.nature.com/reprints>

Publisher's note Springer Nature remains neutral with regard to jurisdictional claims in published maps and institutional affiliations.

Open Access This article is licensed under a Creative Commons Attribution-NonCommercial-NoDerivatives 4.0 International License, which permits any non-commercial use, sharing, distribution and reproduction in any medium or format, as long as you give appropriate credit to the original author(s) and the source, provide a link to the Creative Commons licence, and indicate if you modified the licensed material. You do not have permission under this licence to share adapted material derived from this article or parts of it. The images or other third party material in this article are included in the article's Creative Commons licence, unless indicated otherwise in a credit line to the material. If material is not included in the article's Creative Commons licence and your intended use is not permitted by statutory regulation or exceeds the permitted use, you will need to obtain permission directly from the copyright holder. To view a copy of this licence, visit <http://creativecommons.org/licenses/by-nc-nd/4.0/>.

© The Author(s) 2025